aerospace

MDPI

*Article*

# Characterizations of Swept Shock/Boundary Layer Interactions: A Comparison Between Planar Shock, Curved Shock, and Isentropic Compression

**Fajia Sheng [1,2], Dengxue Song [1], Hexia Huang [1,*], Huijun Tan [1], Xiankai Li [2] and Zhiyu Zhang [2]**

[1] College of Energy and Power Engineering, Nanjing University of Aeronautics and Astronautics, Nanjing 210016, China; sfj636@163.com (F.S.); tanhuijun@nuaa.edu.cn (H.T.)
[2] Yangzhou Collaborative Innovation Research Institute Co., Ltd., Shenyang Aircraft Design and Research Institute, Yangzhou 225000, China; likaixin2378@163.com (X.L.); zhiyu@mail.ustc.edu.cn (Z.Z.)
* Correspondence: huanghexia@nuaa.edu.cn

**Abstract**

To investigate the flow characteristics of three-dimensional swept interactions, 3D steady Reynolds-averaged Navier–Stokes (RANS) simulations are conducted at an incoming Mach number of 3.5 and a Reynolds number of 30,955 based on the incoming boundary-layer thickness $\delta_0$. Three independent compression configurations with a total compression angle of 18° are analyzed and compared: planar swept shocks, curved swept shocks featuring an initial 2° deflection step followed by a continuously curved compression surface, and continuous isentropic compression waves. The results demonstrate that, unlike the baseline planar case, the interactions induced by both curved swept shocks and isentropic compression waves depart from the canonical quasi-conical similarity and transcend existing topological classification frameworks. These non-planar interactions are characterized by large-scale primary vortices and small-scale corner vortices that evolve along curved trajectories downstream. Quantitatively, the curved shock interaction yields maximum normal scales of $5.4\delta_0$ for the primary vortex and $1.8\delta_0$ for the corner vortex—significantly more compact than the $6.7\delta_0$ and $7.5\delta_0$ observed in the planar-shock interaction. Furthermore, the specific modality of compression—whether by discrete shock or continuous wave—exerts a profound effect on aerodynamic performance. Under the present conditions, while isentropic compression achieves the highest compression efficiency and planar shocks provide superior mass flow capture, curved shock compression strikes a favorable balance between these competing metrics. Curved shock configurations may offer potential for improving integrated inlet performance through appropriate adjustment of the initial shock strength.

**Keywords:** three-dimensional swept interactions; quasi-conical similarity; primary vortices; compression efficiency; mass flow capture

Check for updates

Academic Editor: Kung-Ming Chung

Received: 22 March 2026
Revised: 31 May 2026
Accepted: 1 June 2026
Published: 10 June 2026

## 1. Introduction

Swept shock wave/turbulent boundary layer interactions (SSWTBLIs) are ubiquitous in both the internal and external flow fields of supersonic and hypersonic vehicles, frequently occurring at junctions such as fuselage/wing, fuselage/vertical stabilizer, and within propulsion system inlets [1]. Compared to external flows, SSWTBLIs within inlets present more formidable challenges due to the confinement effects of the duct and the complex interplay between multiple interaction regions [2]. These phenomena typically originate from the impingement of external compression shocks from the forebody or

https://doi.org/10.3390/aerospace13060539

internal shocks from the cowl onto the sidewall boundary layers. Sufficiently strong swept shocks induce large-scale, three-dimensional flow separation, resulting in the local accumulation of low-energy fluid and the formation of high-heat-flux zones. These effects severely compromise the aerodynamic performance and structural integrity of the inlet. Furthermore, transverse secondary flows induced by SSWTBLIs at the cowl can evolve into potent corner vortices within the duct, significantly escalating total pressure loss and flow distortion at the engine entrance plane [3]. Consequently, a fundamental understanding of SSWTBLI flow physics and the development of effective flow control strategies are imperative for enhancing the overall performance of high-speed inlets.

To investigate the separation patterns of the SSWTBLI, numerous experimental and numerical simulations have been conducted by researchers worldwide [4–11]. Among these, Alvi and Settles [10,11] employed PLS technology and the shadow method to conduct systematic experimental investigations on SSWTBLI phenomena. Based on the shock normal Mach number $Ma_\mathrm{n}$ = $Ma_0$ sin$\beta_\mathrm{s}$, they categorized such flows into five distinct modes: (1) Non-separated state ($Ma_\mathrm{n} \leq 1.2$); (2) Primary separation state ($1.2 \leq Ma_\mathrm{n} \leq 1.5$); (3) Secondary separation state ($1.5 \leq Ma_\mathrm{n} \leq 1.9$); (4) Normal shock state in the jet region ($1.9 \leq Ma_\mathrm{n} \leq 2.1$); (5) Supersonic backflow state ($Ma_\mathrm{n} \geq 2.1$). These five interaction modes have been corroborated by other experimental and simulation results [12–14]. Token [15] and Kubota [16] subsequently obtained three-dimensional flow models of the SSWTBLI through extensive experimental studies. Their findings indicated that, for the SSWTBLI formed by the fin/plate configuration, the entire interaction region is dominated by a large-scale conical separation vortex located between the separation line and the reattachment line. The separation line lies upstream of the inviscid shock wave, while the reattachment line is close to the corner of the fin/plate. In recent years, with advancements in experimental techniques and simulation methods, scholars worldwide have employed advanced experimental technologies (such as Background-Oriented Schlieren, full-optical imaging, Particle Image Velocimetry (PIV), and Nano-Scale Planar Laser Scattering (NPLS)) and high-precision numerical simulation methods (e.g., Large Eddy Simulation (LES)) to acquire more detailed three-dimensional flow structures of SSWTBLIs [17–21]. Both the flow models proposed by Token [15] and Kubota [16] demonstrated that the large-scale separation vortex on the plate exhibits a conical structure, with its separation line and reattachment line intersecting at a single point upstream of the fin. Subsequently, numerous scholars conducted a series of verifications on the quasi-conical similarity nature of the fin/plate flow [22–30]. The results showed that, except for the initial region immediately adjacent to the leading edge of the fin, the fin/plate flow possesses conical characteristics. The separation line, reattachment line, upstream influence line, and inviscid shock trajectory on the plate surface all converge at the same Virtual Conical Origin (VCO) point upstream of the fin, and the flow parameters along the same ray emanating from the VCO point remain constant.

To investigate the influence of the entropy layer on the SSWTBLI, Borovoy et al. [31] combined experimental and simulation methods to focus on the effects of the entropy layer on heat transfer and pressure characteristics within the SSWTBLI region. Li et al. [32] conducted a study on the fin/blunt plate model using simulation methods and found that the introduction of the entropy layer does not change the inherent quasi-conical similarity nature of the SSWTBLI, nor does it alter the position of the VCO. It only changes the angles of the upstream influence line and separation line.

Compared to the single SSWTBLI, research on the dual-swept shock wave/turbulent boundary layer interactions phenomenon has emerged relatively later. Overseas scholars have primarily investigated cross-double swept shock wave/turbulent boundary layer interactions generated by double fins on opposite sides, revealing separation patterns and three-dimensional flow structures induced by this crossed interaction [33–41]. In contrast, Chinese researchers have mainly focused on the characteristics of ipsilateral dual-swept shock wave/turbulent boundary layer interactions generated by double fins on the same side [42–44]. The research results show that the two interaction regions of the dual-swept shocks/boundary layer interaction flow interfere with each other. Though the interaction region formed by the first swept shock maintains its quasi-conical similarity nature, due to the non-uniform flow downstream of the first shock, the quasi-conical similarity nature is no longer applicable to the second SSWTBLI [42].

The aforementioned review reveals that current SSWTBLI research predominantly centers on interactions involving planar swept shocks (generated by planar compression) and turbulent boundary layers. Scant attention, however, has been devoted to the interaction characteristics involving curved swept shocks (generated by curved compression) or isentropic compression waves. In practical supersonic/hypersonic inlet design, curved surfaces or isentropic compression are frequently employed to mitigate shock intensity and reduce the total pressure loss. These compression systems interact with the sidewall boundary layers, giving rise to curved swept shock or isentropic swept compression wave/boundary layer interactions. Therefore, it is imperative to conduct systematic investigations into the flow physics of interactions involving curved swept shocks, continuous compression waves, and turbulent boundary layers.

In this study, a curved fin/plate configuration is derived from actual inlet geometries to serve as a simplified physical model. Comprehensive investigations are conducted into the interactions between curved-compression swept shocks, continuous compression waves, and turbulent boundary layers. These phenomena are systematically compared with baseline planar SSWTBLI generated by a conventional planar fin/plate model. The objective is to characterize the flow physics of curved compression swept shock wave/continuous compression wave/turbulent boundary layer interaction, evaluate the validity of existing theoretical frameworks, and establish a foundational basis for the aerodynamic design and flow control for high-speed inlets.

## 2. Model Setup and Numerical Approach Validation

### 2.1. Numerical Methods

This study employs the commercial Computational Fluid Dynamics (CFD) software Fluent 2021 R1 to perform three-dimensional numerical simulations. The governing equations are the steady Reynolds-Averaged Navier–Stokes (RANS) equations. The SSWTBLI flow considered in this study exhibits complex flow features, including strong turbulence anisotropy, flow separation, and shock-induced pressure gradients. Linear eddy-viscosity models based on the Boussinesq hypothesis, such as the k–ω SST model, have been successfully applied to similar flows. However, their inherent assumption of isotropic turbulence may limit their predictive capability in flows with pronounced anisotropy, streamline curvature, and shock–boundary-layer interactions. To better capture these effects, the Reynolds Stress Model (RSM) with the stress–ω formulation is adopted. This model belongs to the class of second-moment closure (SMC) models, in which transport equations are solved directly for all independent components of the Reynolds stress tensor, together with a transport equation for the specific dissipation rate $\omega$. Although the Reynolds stress transport equations are derived from exact moment equations, higher-order correlations (e.g., pressure–strain interactions and turbulent diffusion) are not explicitly solved but are modeled using established closure formulations. Compared with linear eddy-viscosity models, the RSM provides improved capability in representing turbulence anisotropy and complex stress–strain interactions.

The transport equations for the Reynolds stresses can be written in the general form:

$$\frac{\partial\left(\rho\overline{u_i'u_j'}\right)}{\partial t}+\frac{\partial\left(\rho\overline{u_k}\overline{\mu_i'\mu_j'}\right)}{\partial x_k}=P_{ij}+\Phi_{ij}+\varepsilon_{ij}+D_{ij} \tag{1}$$

where $P_{ij}$, $\Phi_{ij}$, $\varepsilon_{ij}$, and $D_{ij}$ denote the production, pressure-strain redistribution, dissipation, and diffusion terms, respectively. In the present study, the pressure-strain and diffusion terms are modeled using the standard formulations implemented in ANSYS Fluent 2021 R1, and the dissipation term is assumed to be isotropic. The turbulence scale is obtained from the transport equation for the specific dissipation rate $\omega$.

For the numerical discretization, the convective fluxes are computed using the Roe flux-difference splitting scheme. A second-order upwind scheme is employed for spatial discretization of the governing equations. An implicit formulation is used to accelerate convergence. The molecular viscosity is evaluated using Sutherland's law.

Structured hexahedral meshes were generated for the computational domain using ANSYS ICEM CFD 2021 R1. To satisfy the near-wall $y^+$ requirements of the turbulence model and ensure shock capturing, local grid refinement was implemented in the near-wall regions and around the shock structures. A no-slip, adiabatic wall condition was assigned to all solid surfaces. The inflow conditions were prescribed using a velocity-inlet boundary, where spanwise-consistent boundary layer profiles were mapped via a user-defined profile method. A pressure-outlet condition was applied at the exit plane, with the static pressure maintained at the free-stream value. Symmetry boundary conditions were enforced on the lateral and upper surfaces of the domain. During the simulation, the mass flow rate, area-weighted average pressure, and Mach number at the computational domain exit were closely monitored. Numerical convergence was confirmed once the monitored parameters reached a statistically steady state.

It should be noted that all solid walls in the present simulations are modeled as adiabatic walls. Therefore, the present study focuses on the aerodynamic flow structures, shock wave/boundary-layer interaction characteristics, and inlet aerodynamic performance of different compression configurations, rather than on a coupled aerodynamic-thermal analysis. Consequently, wall heat flux is not directly predicted, and no quantitative assessment of the thermal-protection system is provided. The discussion of high-heat-flux regions and thermal-protection implications is intended only to highlight potential engineering concerns associated with such flow structures.

### *2.2. Numerical Approach Validation*

According to studies by Alvi and Settles [11], primary separation and secondary separation represent the primary interaction phenomena generated by SSWTBLIs. The accuracy of numerical simulations for these two interaction phenomena directly impacts the reliability of simulation methods, particularly for secondary separation. Currently, only a few specially modified RANS models and high-precision simulations can reproduce this phenomenon [14,45,46]. To validate the accuracy of the simulation method presented in this paper, separate verification tests must be conducted for both primary and secondary separation interaction modes.

- Validation case 1: Primary Separation Interaction Mode

The SSWTBLI experiment reported in ref. [25] was conducted in the primary-separation interaction regime and was therefore selected as the validation case for primary separation. Figure 1 shows the main geometric dimensions of the experimental model and the locations of the measurement points. The freestream Mach number in the experiment was 2.91, and the incoming boundary-layer thickness was $\delta_0$ = 5 mm. The detailed experimental flow conditions are listed in Table 1. The pressure and temperature values listed in the table denote the total pressure and total temperature, respectively, corresponding to the wind-tunnel experimental conditions reported in ref. [25]. Figure 2 displays the wall-boundary limit streamlines obtained from the simulation. Solid lines of different colors simultaneously mark the positions of surface characteristic lines. It can be observed that the simulation successfully captures the primary separation phenomenon. Furthermore, the upstream influence line, separation line, and reattachment line obtained from the simulation intersect at the same point VCO, consistent with the quasi-conical similarity characteristics of the SSWTBLI. The experiment meticulously measured the yaw angle and pitot pressure distribution across six stack positions. Figure 3 compares CFD simulation results with experimental data. Each plot includes a scaled reference for yaw angle and pitot pressure, with the origin of each stack position aligned to the blue vertical line on the horizontal axis. The figure demonstrates that the simulated yaw angles and pitot pressures, particularly within the interaction region, agree very well with the experimental results.

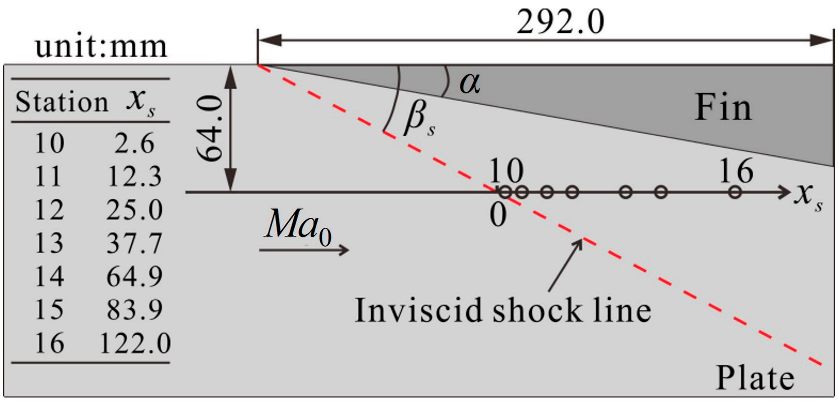

**Figure 1.** Sketch of the sharp fin and the measurement point positions in ref. [25].

**Table 1.** Incoming flow conditions of the experiment in ref. [25].

| $\delta_0$ [mm] | $Ma_0$ | $\alpha$ [°] | $Re_{\delta 0}$ | $Pt_0$ [Pa] | $Tt_0$ [K] |
|---|---|---|---|---|---|
| 5 | 2.91 | 10 | $3.04 \times 10^5$ | 689,700 | 275.9 |

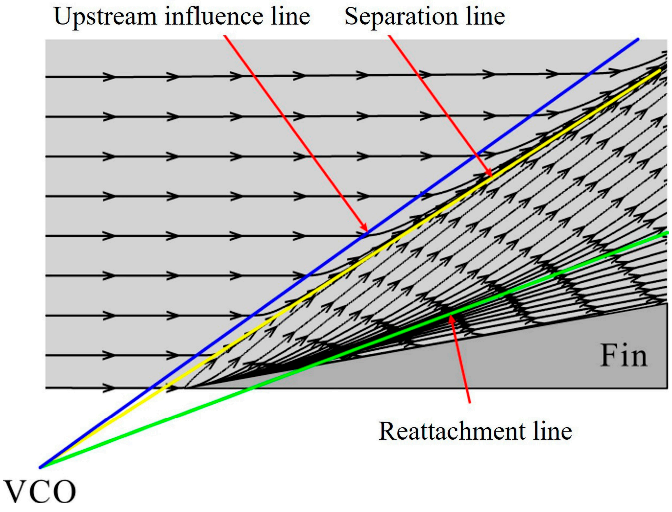

**Figure 2.** CFD predicted skin-friction lines at the bottom wall (primary separation pattern).

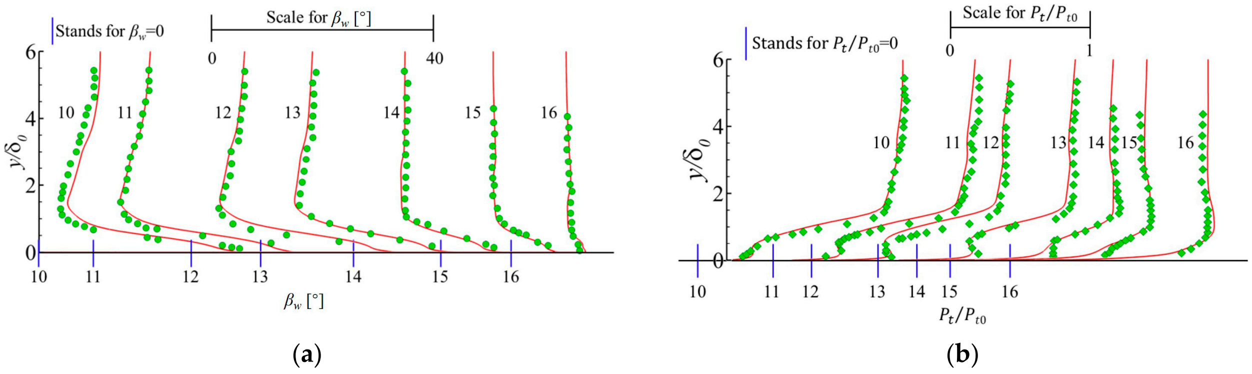

**Figure 3.** Numerical and experimental results comparison (red solid line: CFD results, symbols: experimental results). (**a**) Yaw angle comparisons. (**b**) Pitot pressure comparisons.

- Validation case 2: Secondary Separation Interaction Mode

The experimental condition reported in ref. [29], with a freestream Mach number of 3.03 and a fin compression angle of 16°, corresponds to the secondary-separation interaction regime. Therefore, this condition was selected as the validation case for secondary separation. Figure 4 shows the main geometric dimensions of the experimental model and the locations of the measurement points for this condition, while the detailed experimental flow conditions are listed in Table 2. The pressure and temperature values listed in the table denote the total pressure and total temperature, respectively, corresponding to the wind-tunnel experimental conditions reported in ref. [29]. This experiment employed both pressure measurement and a Laser Interferometer Skin Friction (LISF) tester to comprehensively measure the distribution of wall static pressure and wall friction coefficient. Figure 5 displays the wall-boundary limit streamlines obtained from the CFD simulation. The simulation successfully captures the secondary separation phenomenon, with the secondary separation line and secondary reattachment line intersecting at the same point VCO with other characteristic lines, consistent with quasi-conical similarity characteristics. Figure 6 compares CFD simulation results with experimental data. The figure shows that both the simulated wall-boundary static pressure and friction coefficient exhibit good agreement with experimental results.

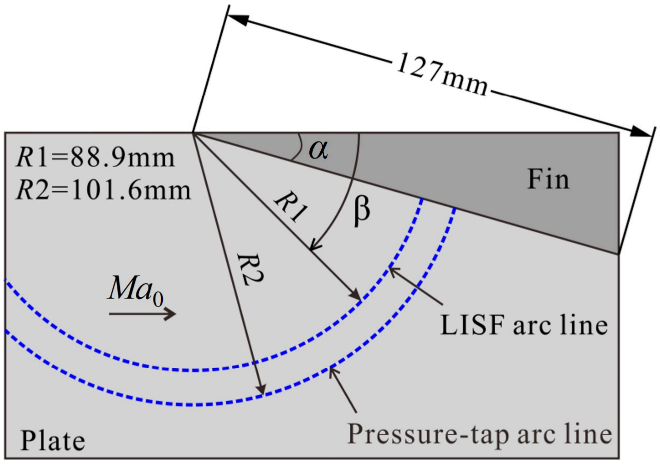

**Figure 4.** Sketch of the experimental model and the measurement point positions in ref. [29].

**Table 2.** Incoming flow conditions of the experiment in ref. [29].

| $\delta_0$ [mm] | $Ma_0$ | $\alpha$ [°] | $Re_{\delta 0}$ | $Pt_0$ [Pa] | $Tt_0$ [K] |
|---|---|---|---|---|---|
| 3.02 | 3.03 | 16 | $1.88 \times 10^5$ | 827,000 | 293.5 |

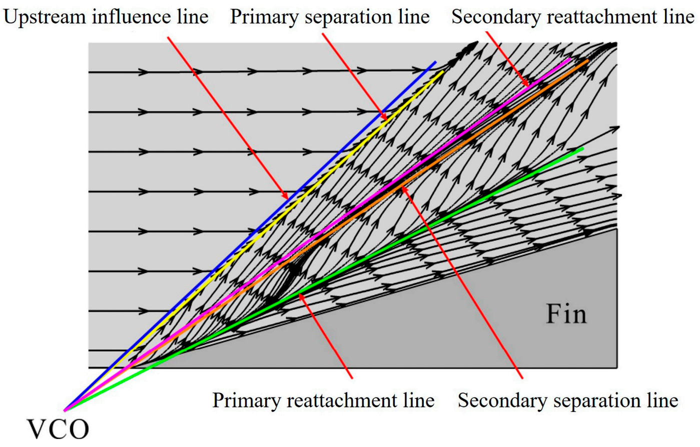

**Figure 5.** CFD predicted skin-friction lines at the bottom wall (secondary separation pattern).

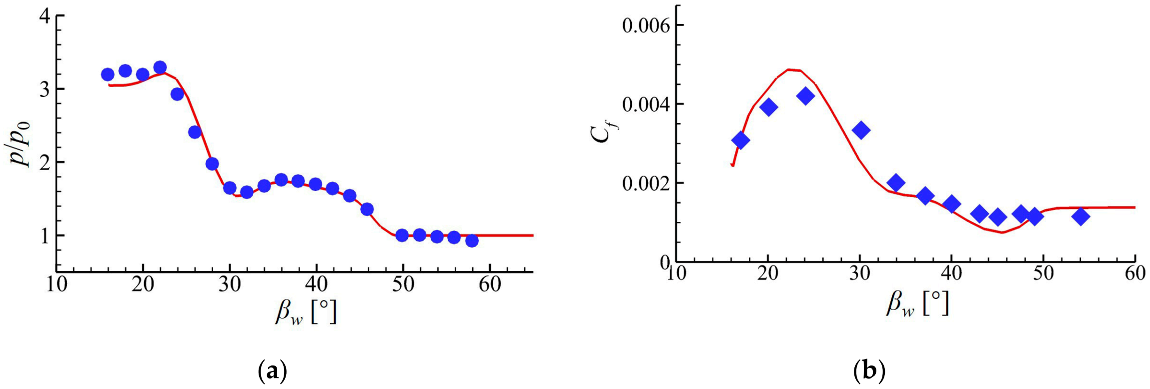

**Figure 6.** Numerical and experimental results comparisons (red solid line: CFD results, symbols: experimental results). (**a**) Wall pressure comparisons. (**b**) Wall friction coefficients comparisons.

Based on the validation results from primary separation and secondary separation cases, it is evident that the simulation method employed in this paper can accurately capture the complex interaction between swept shock waves and turbulent boundary layers. This approach can be utilized to advance subsequent research in this study.

### 2.3. Model Setup

To investigate the flow physics of curved-compression SSWTBLIs, three distinct fin-plate configurations were developed, as illustrated in Figure 7. Figure 7a presents the baseline planar swept shock/boundary layer interaction model, comprising a sharp fin with a constant deflection angle of 18°. The supersonic inflow is deflected by the fin, generating a planar oblique shock wave. The impingement of this shock onto the turbulent boundary layer developing on the plate induces the canonical 3D SSWTBLI. Figure 7b illustrates the curved swept shock/boundary layer interaction model, where the fin deflection angle evolves continuously from an initial 2° to a final 18°. As the supersonic flow undergoes compression along the curved surface, a weak initial oblique shock is formed, which subsequently coalesces with a series of isentropic compression waves. This process results in a downstream-curving shock front that interacts with the boundary layer, creating a curved SSWTBLI. Figure 7c shows the isentropic swept compression/boundary layer interaction model. In this configuration, the fin deflection angle starts at 0° and increases monotonically to 18° via a continuous curved profile. The inflow is compressed gradually, generating a fan of isentropic compression waves designed to converge at a prescribed downstream focal point. This configuration specifically targets the interaction between diffuse isentropic compression waves and the turbulent boundary layer.

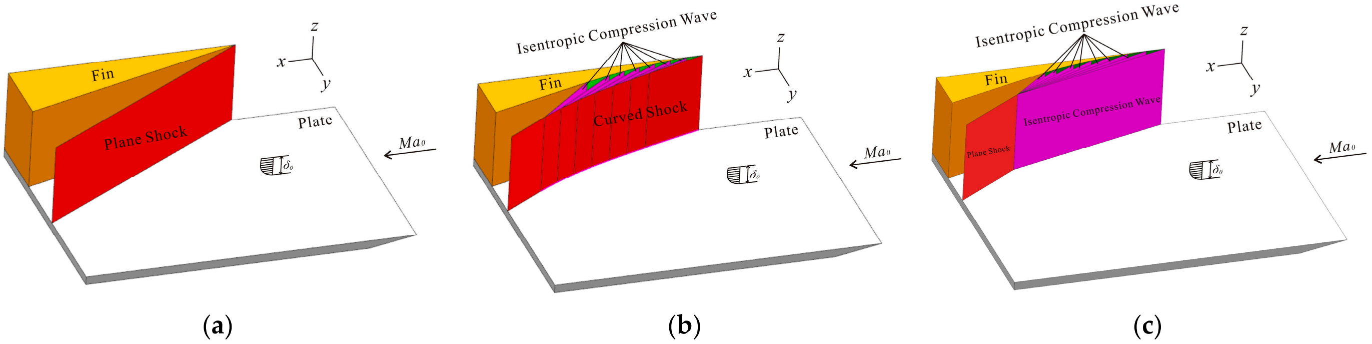

**Figure 7.** Swept shock wave (continuous compression waves)/turbulent boundary layer interaction geometric models. (**a**) Planar swept shock model. (**b**) Curved swept shock model. (**c**) Isentropic swept compression waves model.

In the present work, the term “isentropic compression” is used in a restricted sense. It refers only to the shock-free continuous compression wave region in the off-wall inviscid core flow before wave coalescence. This region is induced by the smooth concave compression surface and can be modeled as a continuous sequence of infinitesimal Mach waves or very weak compression waves; therefore, under the inviscid approximation, it may be locally treated as isentropic. This term does not apply to the near-wall viscous region or to the downstream concentrated shock formed by the coalescence of compression waves, where irreversibility and entropy generation occur.

The computational domain dimensions of the curved compression model are shown in Figure 8, and the same domain dimensions are used for the other two models. The incoming boundary layer thickness at the inlet, $\delta_0$, is set to 5 mm. To minimize the influence of the top and lateral boundaries on the flow in the interaction region, the domain height and spanwise width are set to $H = 40\delta_0$ and $W = 120\delta_0$, respectively. The streamwise lengths of Symmetry Plane 1, the curved compression surface, and the planar compression surface are $L_0 = 10\delta_0$, $L_1 = 60\delta_0$, and $L_2 = 50\delta_0$, respectively, giving a total streamwise length of $120\delta_0$.

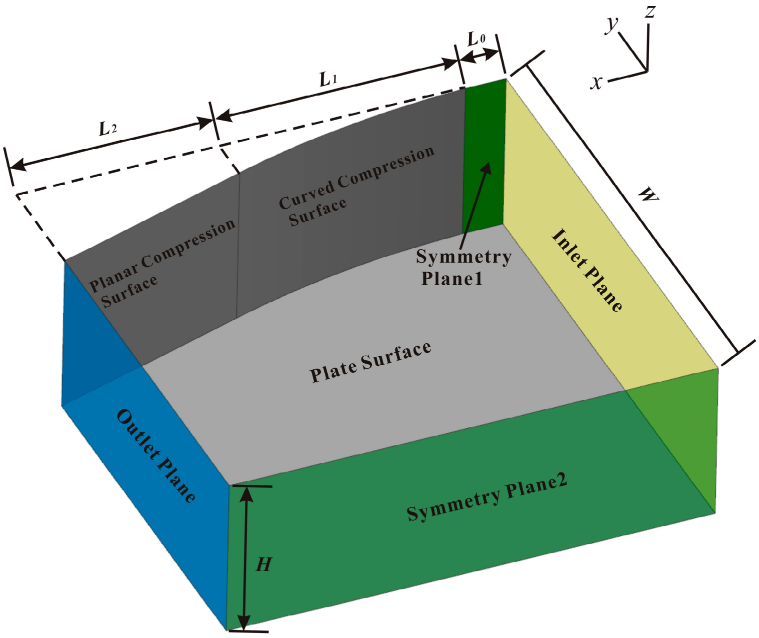

**Figure 8.** Computational domain dimensions. (Curved shock compression).

### 2.4. Computational Flow Conditions

For the three simulation cases mentioned above, the freestream Mach number is 3.5, the freestream total pressure and total temperature are 101,325 Pa and 288.15 K, respectively. The freestream boundary layer thickness is $\delta_0$ = 5 mm, which is adopted as the reference length in the present study. Accordingly, the Reynolds number is defined as

$$Re_{\delta_0} = \frac{\rho_0 u_0 \delta_0}{\mu_0} \tag{2}$$

where $\rho_0$, $u_0$, and $\mu_0$ are the freestream density, velocity, and dynamic viscosity, respectively. The detailed flow conditions and numerical parameters are summarized in Table 3. It should be noted that $Pt_0$ and $Tt_0$ in Table 3 denote the inlet total pressure and inlet total temperature, respectively. The condition listed in Table 3 corresponds to the experimental condition of the supersonic wind tunnel NHS at Nanjing University of Aeronautics and Astronautics. Since this facility is a vacuum-suction free-jet supersonic wind tunnel, the freestream total pressure and total temperature correspond to the ambient pressure and temperature during the experiment, respectively. Therefore, the condition in Table 3 is mainly used to characterize the subsequent wind-tunnel experimental condition.

**Table 3.** Incoming flow conditions for computations.

| Parameter | Value |
|---|---|
| $Ma_0$ | 3.5 |
| $Pt_0/\mathrm{Pa}$ | 101,325 |
| $Tt_0/\mathrm{K}$ | 288.15 |
| $Re_{\delta 0}$ | 30,955 |

In the present simulation, the inlet velocity boundary condition was imposed using a prescribed profile, which was obtained from the Reynolds stress turbulence model described in Section 2.1. The corresponding velocity, turbulent kinetic energy, specific dissipation rate, and Reynolds stress profiles of the incoming boundary layer are shown in Figure 9. The boundary layer displacement thickness is 2.4 mm, yielding a Reynolds number based on the displacement thickness of 14,960.

Structured multi-block grids were generated for all three configurations. The grid was refined in the near-wall region, the expected shock interaction region, and around the curved compression surface to accurately capture the boundary layer development, shock structures, and compression wave evolution. The total number of grid cells for the final mesh of each model is approximately 17 million. Figure 10a shows the wall, symmetry plane, and inlet grid distributions for the curved swept shock/boundary layer interaction model. The grid topologies for the other models in this paper are similar.

To ensure adequate near-wall resolution, the first grid layer height was set to 0.01 mm, which was carefully selected to maintain the wall-normal dimensionless distance $y^+$ below 1 over the main interaction region, as shown in Figure 10b. Here, $y^+$ denotes the dimensionless wall-normal distance calculated based on the local normal distance from each wall surface, rather than a distance measured along a fixed global coordinate direction. Therefore, for the curved compression surface, the wall-normal distance is determined along its local normal direction. As for the flat plate, the wall-normal direction coincides with the z-direction, i.e., the $y^+$ stands for $z^+$. As $y^+$ also depends on the local friction velocity and near-wall kinematic viscosity, values much smaller than 1 may occur locally even with a uniform first grid-layer height. Similar $y^+$ magnitudes and distributions were obtained for the other two configurations. This indicates that the viscous sublayer is sufficiently resolved in all configurations, which is essential for the present Reynolds stress model calculations and for the accurate prediction of near-wall flow structures and turbulent boundary-layer responses. A consistent mesh resolution was adopted in the near-wall and main interaction regions for the three configurations to ensure a reliable quantitative comparison.

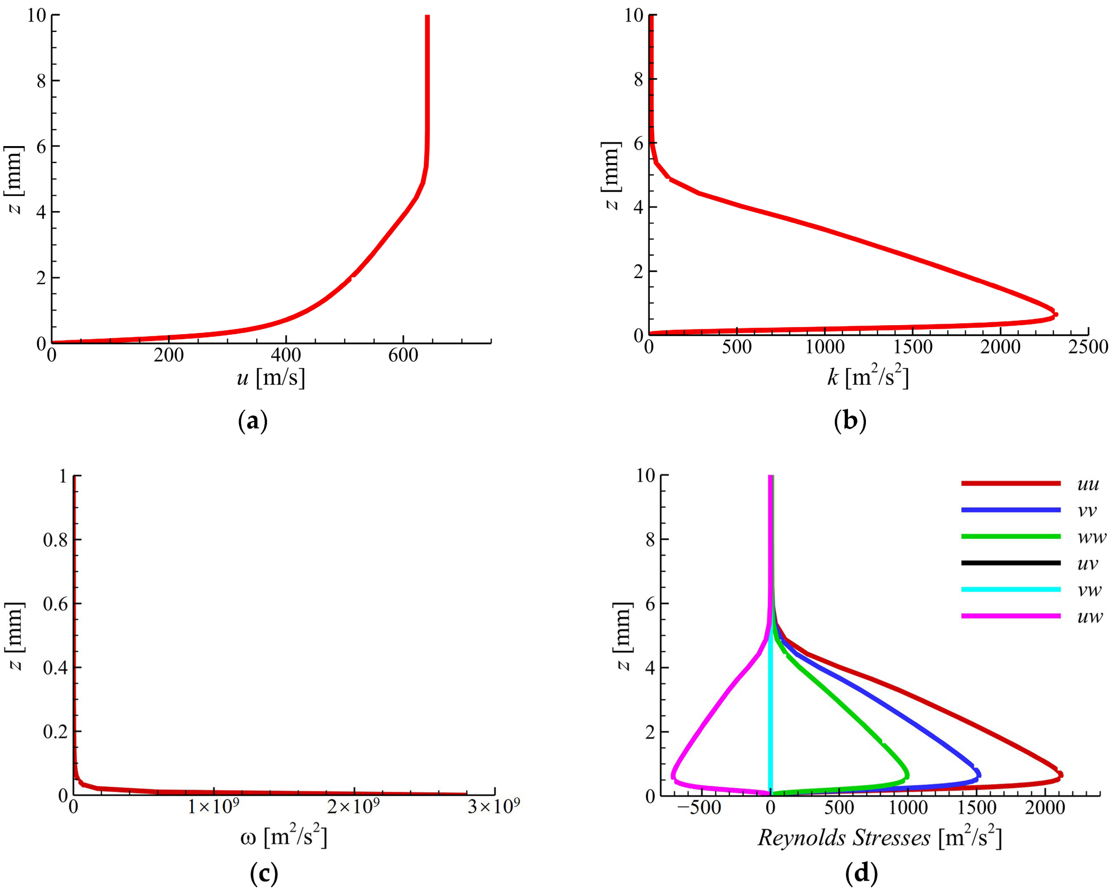

(**a**) (**b**)

(**c**) (**d**)

**Figure 9.** Incoming boundary layer profile. (**a**) Velocity. (**b**) Turbulent kinetic energy. (**c**) Specific dissipation rate. (**d**) Reynolds stresses.

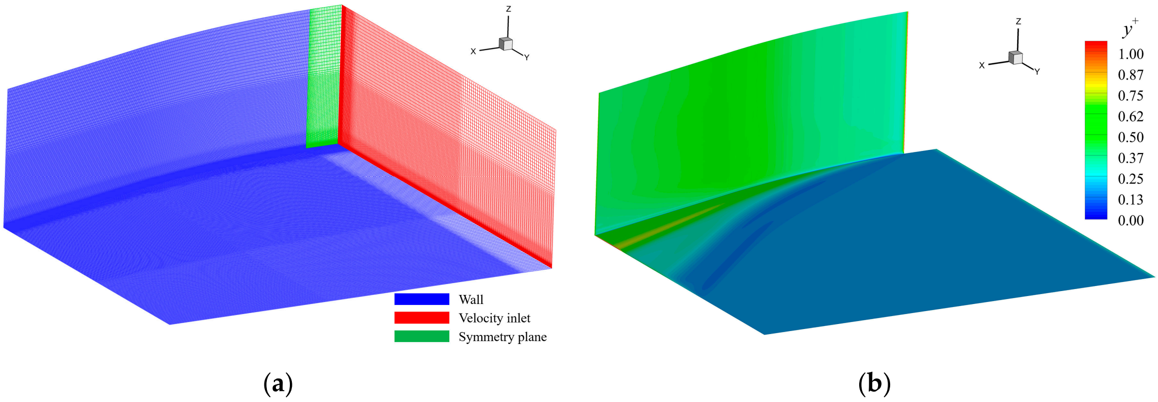

(**a**) (**b**)

**Figure 10.** Computational Surface meshes and Distribution of the local dimensionless wall-normal distance $y^+$. (Curved shock compression). (**a**) Computational Surface meshes. (**b**) Distribution of the local dimensionless wall-normal distance $y^+$ (stands for $z^+$ on the flat plate).

A grid-independence study was also conducted to evaluate the sensitivity of the numerical results to grid resolution. Three grids with increasing cell counts were generated, namely a coarse mesh with approximately 10 million cells, a fine mesh with approximately 17 million cells, and a dense mesh with approximately 24 million cells. The wall pressure and wall friction coefficient distributions obtained using the three grids were compared, as shown in Figure 11. The results show that the differences between the fine and dense grids are negligible for both the wall pressure and wall friction coefficient distributions. Therefore, the fine mesh with approximately 17 million cells was adopted for the present simulations, as it provides a suitable balance between numerical accuracy and computational cost.

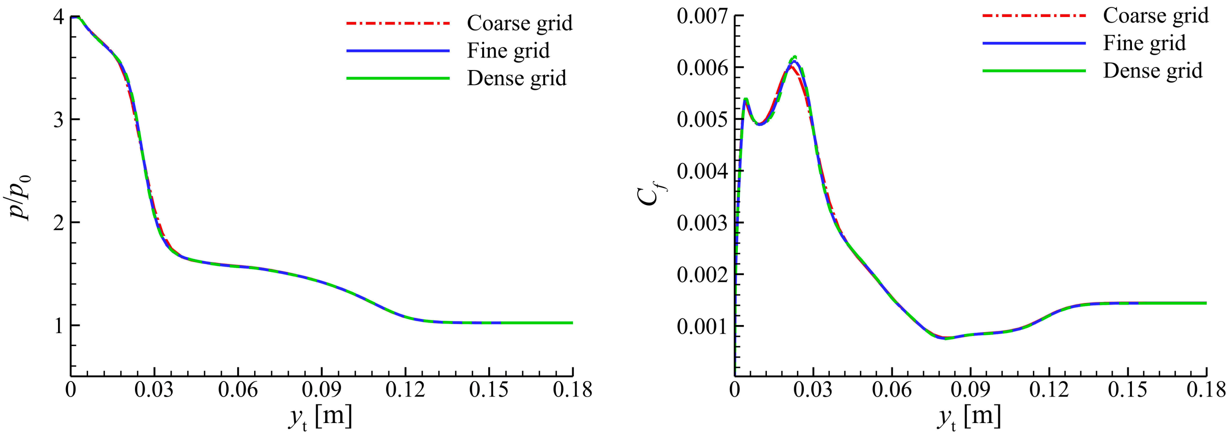

(**a**) (**b**)

**Figure 11.** Wall pressure and wall friction coefficient distributions for different grids (The intersection line of the x = 300 mm cross-section, perpendicular to the compression surface, with the plate surface). (**a**) Wall pressure. (**b**) Wall friction coefficient.

The computational cost of the present simulations was also evaluated. For a single case with approximately 17 million cells using the Reynolds stress model, the calculation required about 16 h on a workstation equipped with 32 CPU cores and 256 GB of memory. This information is provided to clarify the computational scale and resource requirements of the present numerical simulations.

## 3. Results and Discussion

### 3.1. Inviscid Flow Field Structure and Flow Separation Mode

Figure 12 illustrates the inviscid flow topologies associated with the three swept compression configurations. The inviscid flow for the planar-compression case is relatively straightforward, characterized by a planar swept shock. In contrast, the curved-compression flow field exhibits a more complex structure, comprising a curved shock front, a fan of isentropic compression waves originating from the curved surface, and a resultant coalesced shock followed by a slip surface emanating from the coalescence point. Similarly, in the isentropic compression case, the compression waves are designed to focus at a singular focal point, subsequently forming a concentrated shock wave and a corresponding slip surface downstream. To quantify the pressure rise characteristics across these three configurations, two probing lines (Line 1 and Line 2), oriented normal to the compression surface, were extracted from the core inviscid flow field, as indicated by the blue dashed lines. The streamwise locations of the intersections between these probes and the compression surface are specifically labeled in the figure.

Figure 13 displays the static pressure distributions along Line 1 and Line 2 for the three investigated configurations. In the planar-compression case, the pressure profile manifests a sharp discontinuity upon crossing the shock front, characterized by an abrupt, step-like increase in the pressure ratio. For the curved-compression configuration, the overall compression occurs in two distinct stages: a discrete pressure jump across the initial curved shock, followed by a continuous isentropic rise. The pressure increment attributed to the curved shock surpasses that of the isentropic portion, yielding a profile that exhibits a steep initial gradient before transitioning to a gradual increase. In contrast, the isentropic configuration achieves compression solely through a continuous wave fan, resulting in a monotonic and gradual pressure increase. The pressure profiles downstream of the shock/wave coalescence are compared in Figure 13b. Results indicate that the final pressure ratio attained after complete coalescence is virtually identical across all three configurations. Consequently, given a consistent total deflection angle, the asymptotic inviscid pressure ratio remains invariant regardless of the compression modality, reaching a value of approximately 4.0.

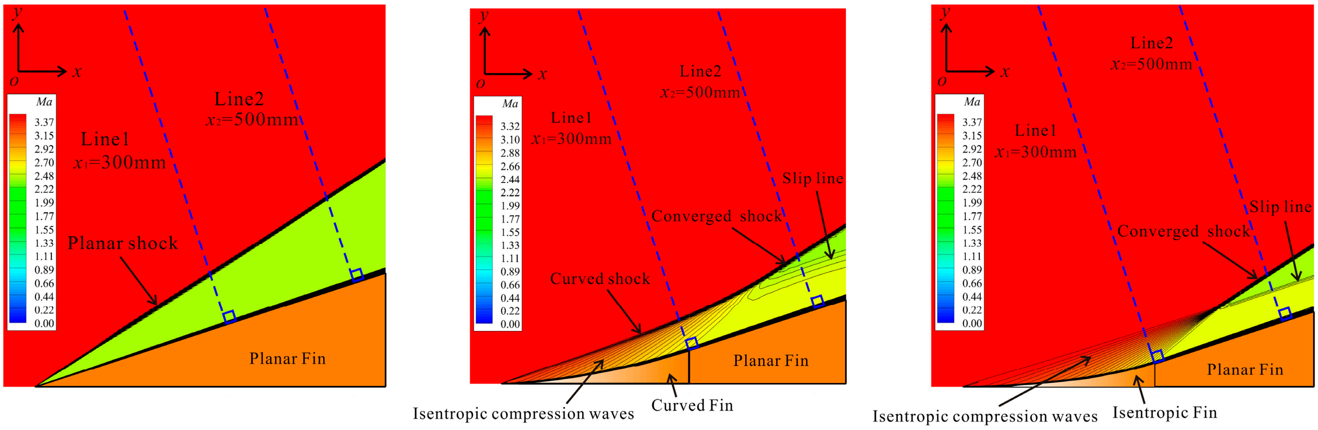

(**a**) (**b**) (**c**)

**Figure 12.** Inviscid flowfield structures Comparison. (**a**) planar shock compression. (**b**) curved shock compression. (**c**) Isentropic compression.

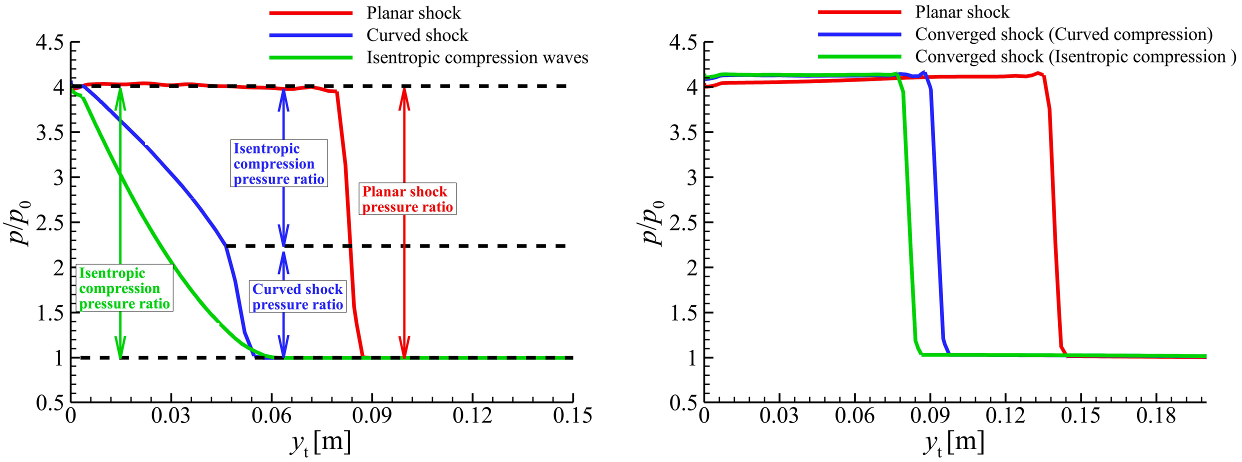

(**a**) (**b**)

**Figure 13.** Pressure rise curves comparison. (**a**) Line 1. (**b**) Line 2.

As analyzed above, when the total compression angle is identical, the inviscid pressure ratios formed by the three compression configurations are essentially the same ($p_{\max}/p_0$ = 4.0). From the pressure ratio relationship given by Equation (1) before and after the oblique shock wave, it can be seen that the equivalent shock wave intensity ($Ma_n = M_0 \sin\beta_s$) for the three compression configurations is also largely comparable. According to the classification of the SSTBLI proposed by Alvi and Settles [10,11], when $1.5 \leq Ma_n \leq 1.9$, the interaction exhibits a secondary separation interaction mode. Substituting $p_2/p_1$ = 4.0 into Equation (2) yields an equivalent shock intensity $Ma_n$ = 1.89 for all three compression configurations. Therefore, when the total compression angle is 18°, the interaction patterns formed by the three compression configurations should theoretically all be in a secondary separation state.

$$\frac{p_2}{p_1} = \frac{2k}{k+1} Ma_1^2 sin^2 \beta_s - \frac{k-1}{k+1} \tag{3}$$

$$Ma_n = \sqrt{\left(\frac{p_2}{p_1} + \frac{k-1}{k+1}\right)\frac{k+1}{2k}} \tag{4}$$

For the curved swept shock wave, the initial shock intensity can be calculated based on an initial compression angle of 2° as $Ma_\mathrm{n}$ = $M_0\sin\beta_\mathrm{s}$ = 1.08. For isentropic swept compression waves, since the initial compression angle is 0°, the initial shock intensity $Ma_\mathrm{n}$ = 0. According to the classification by Alvi and Settles [10,11], when $Ma_\mathrm{n}$ < 1.2, the SSWTBLI is theoretically in a non-separated state. Therefore, the initial interaction patterns formed by curved compression and isentropic compression should theoretically remain in a non-separated state.

In summary, the theoretical interaction pattern for planar swept shock/boundary layer interaction should be a "secondary separation" state. For curved swept shock/boundary layer interaction and isentropic swept compression wave/boundary layer interaction, the theoretical interaction pattern should transition gradually from an initial "non-separated" state to a "secondary separation" state.

Figure 14 simultaneously presents the wall limiting streamlines formed by three types of SSWTBLIs. The solid red lines represent inviscid shocks, while the dashed red lines denote isentropic compression waves. The solid green, blue, and yellow lines, respectively, represent the upstream influence line, the primary separation line, and the primary reattachment line. The solid orange and purple lines represent the secondary separation line and reattachment line, respectively. The upstream influence line is constructed by connecting the points where deflection of the upstream surface boundary streamlines begins.

As shown in Figure 14a, the planar swept shock/boundary layer interaction produces primary and secondary separations, consistent with the classification theory of Alvi and Settles [10,11]. The inviscid shock line, upstream influence line, primary separation line, primary reattachment line, secondary separation line, and secondary reattachment line all intersect at a single point (VCO). According to Settles and Lu [27], this fundamentally reflects the quasi-conical similarity characteristics inherent in this three-dimensional flow.

For the curved swept shock wave/boundary layer interaction in Figure 14b, the entire interaction region can be divided into two parts: the upstream curved shock wave interaction region and the downstream converging shock wave interaction region. Within the curved shock wave interaction region, primary separation occurs, but the inviscid curved shock wave, upstream influence line, separation line, and reattachment line are all curves, with the slope of these curves gradually increasing downstream. The inviscid shock wave, upstream influence line, and reattachment line no longer intersect at a single point, so the characteristic of conical similarity is no longer exhibited. Within the converging shock wave interaction region, a large-scale conical primary separation phenomenon is formed, and the inviscid shock wave line, upstream influence line, separation line, and reattachment line all intersect at a single point (VCO). Consequently, the converging swept shock wave interaction region exhibits conical similarity characteristics. The entire interaction region of the curved swept shock wave/boundary layer interaction is in a "primary separation" state, and there is no transition from the initial "non-separation" to "secondary separation" state, which is inconsistent with the interaction mode classification theory proposed by Alvi and Settles [10,11].

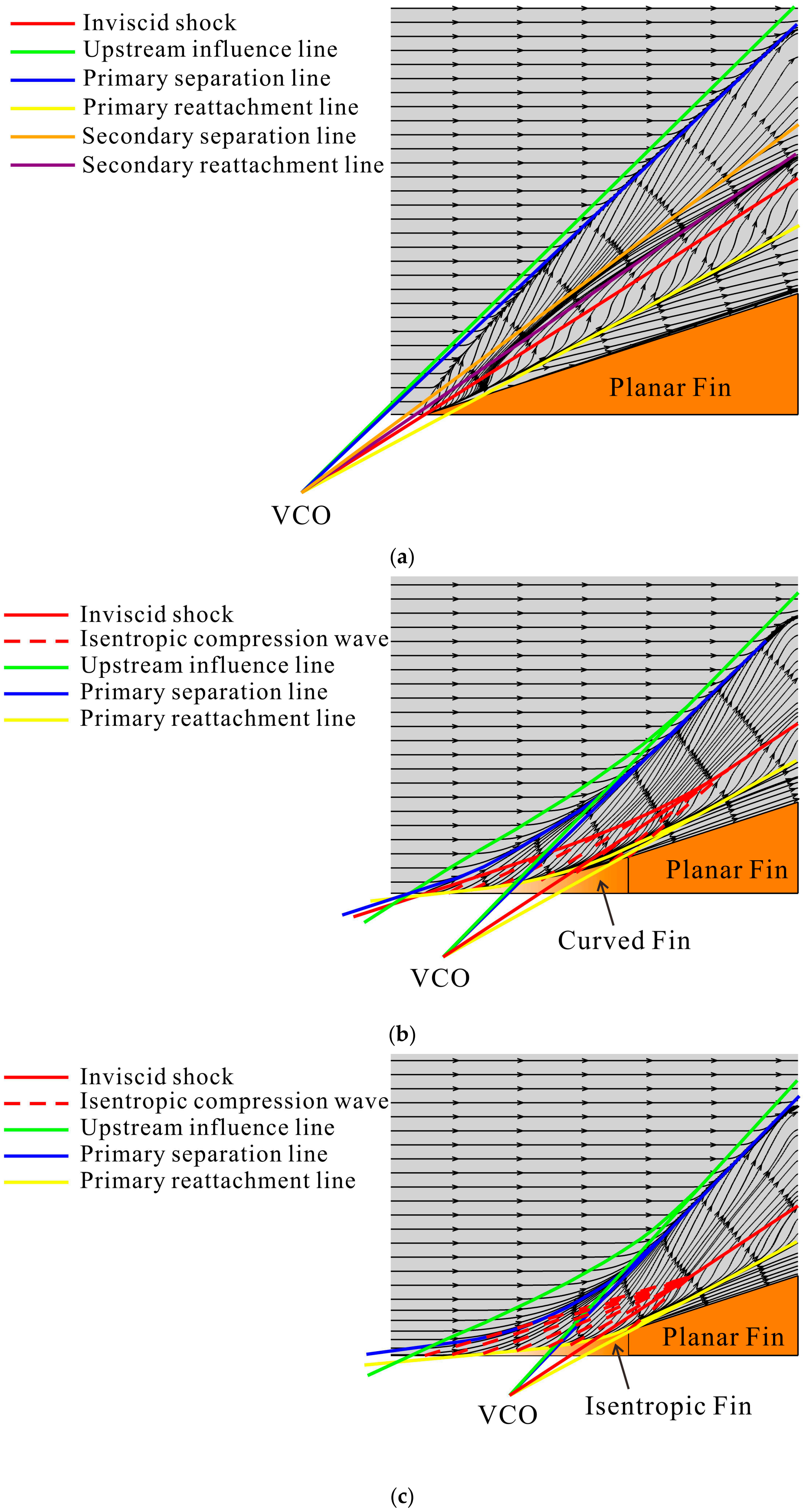

**Figure 14.** Comparison of surface flow patterns. (**a**) Planar swept shock/turbulent boundary layer interaction. (**b**) Curved swept shock/turbulent boundary layer interaction. (**c**) Isentropic swept compression wave/turbulent boundary layer interaction.

https://doi.org/10.3390/aerospace13060539

For the isentropic swept compression wave/boundary layer interaction in Figure 14c, the entire interaction region can be divided into two parts: the upstream isentropic swept compression wave interaction region and the downstream converging shock wave interaction region. Within the isentropic swept compression wave interaction region, primary separation occurs, but the degree of convergence of the wall-limiting streamlines is relatively weaker and the size of the separation region is smaller. All characteristic lines in the interaction region are also curves and no longer intersect at a single point, so the feature of conical similarity is not exhibited either. Within the converging shock wave interaction region, a large-scale conical primary separation phenomenon is formed, and all characteristic lines intersect at a single point (VCO); therefore, this converging swept shock wave interaction region also has the characteristic of conical similarity. The entire interaction region of the isentropic swept compression wave/boundary layer interaction also remains in a "primary separation" state, failing to form a transitional state from initial "non-separation" to "secondary separation", which is also inconsistent with the theory proposed by Alvi and Settles [10,11].

It should be noted that the theory proposed by Alvi and Settles [10,11] was originally developed mainly for discrete swept shock/boundary layer interactions, where the boundary layer is subjected to a concentrated and abrupt pressure rise induced by a swept shock. For the curved swept shock configuration and the continuous swept compression wave configuration investigated in the present study, the compression process accumulates gradually in the streamwise direction, and the boundary layer experiences a spatially distributed pressure-gradient history rather than an abrupt, strong compression induced by a single discrete shock. Therefore, the discrepancy between the present results and the classification criterion does not necessarily imply a complete failure of the equivalent shock scaling itself. Instead, it indicates that, for spatially distributed compression flows, the final pressure ratio or equivalent normal Mach number alone is insufficient to determine the separation topology. The local compression strength, pressure gradient distribution, and boundary-layer response to gradual compression are also important controlling factors affecting the separation mode.

Furthermore, comparative analysis reveals that the separation region formed by planar swept shock wave/boundary layer interaction exhibits the largest scale, followed by curved shock, with the isentropic compression wave producing the smallest scale.

Since the planar oblique shock in Figure 14a and the converging oblique shocks in Figure 14b,c exhibit quasi-conical similarity, a spherical coordinate system with the VCO as the origin, as shown in Figure 14, can be employed to describe such flows. Figure 15 presents the wall pressure distribution induced by SSWTBLI, where the abscissa $\beta$ denotes the azimuthal angle, the ordinate $\mathrm{p/p_0}$ represents the pressure ratio, and $R$ is the radial distance measured from the VCO along the inviscid shock direction. It can be observed that the pressure distribution curves at different radial positions nearly coincide, further confirming the quasi-conical similarity of both the planar and converging SSWTBLI.

Figure 16 presents the wall pressure distributions in the upstream curved shock interaction region of Figure 14b and the upstream isentropic compression wave interaction region of Figure 14c. The curves are plotted in a spherical coordinate system with the VCO as the origin, where the VCO location is determined by the intersection of the upstream tangent to the curved shock or isentropic compression wave with the upstream influence line. It can be observed that the pressure distribution curves at different radial positions do not coincide, indicating that the curved SSWTBLI and the isentropic swept compression wave/turbulent boundary layer interaction no longer exhibit quasi-conical similarity.

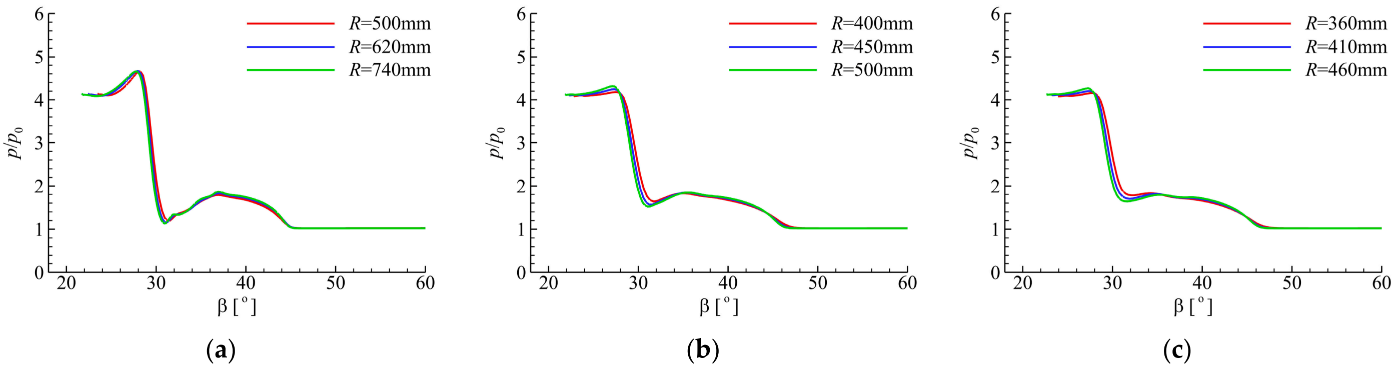

**Figure 15.** Wall pressure distributions. (**a**) Planar SSWTBLI region. (**b**) Converging shock interaction region in the curved shock compression configuration. (**c**) Converging shock interaction region in the isentropic compression configuration.

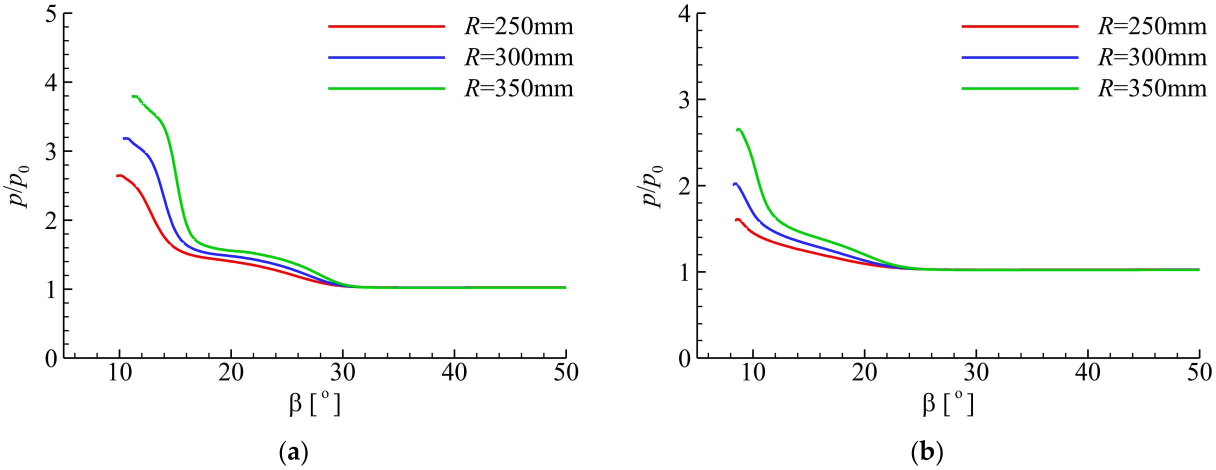

**Figure 16.** Wall pressure distributions. (**a**) Curved shock wave interaction region. (**b**) Isentropic swept compression waves interaction region.

### 3.2. Three-Dimensional Vortex Structure and Lateral Flow Structure

Figure 17 compares the three-dimensional vortical structures in different interaction regions visualized using the Q-criterion. The $Q$ value is nondimensionalized by the freestream velocity and the incoming boundary-layer thickness, as follows:

$$Q^* = \frac{Q}{(u_0/\delta_0)^2} = \frac{Q{\delta_0}^2}{{u_0}^2} \tag{5}$$

where $Q$ is the dimensional $Q$-criterion value, $u_0$ is the freestream velocity, and $\delta_0$ is the incoming boundary layer thickness. In Figure 17, all $Q$-criterion iso-surfaces are plotted at $Q^* = 6.08 \times 10^{-5}$.

As shown in Figure 17a, the planar swept shock/boundary layer interaction generates a large-scale conical vortex structure on the plate surface, while a small-scale corner vortex forms in the corner region between the fin and plate. This result agrees with the findings of Kubota and Stollery [16]. For curved swept shock/boundary layer interaction, the vortex structure in the interaction region primarily consists of an upstream curved shock compression vortex and a downstream converging main vortex. Simultaneously, a small-scale corner vortex forms in the corner region between the fin and the plate. The curved shock compression vortex develops downstream in a curved manner, while the converging main vortex develops conically toward the downstream. For isentropic swept compression wave/boundary layer interaction, the vortex structure consists of an upstream compression wave/boundary layer interaction vortex and a downstream converging main vortex. Similarly, a small-scale corner vortex forms in the corner region between the fin and the plate. The compression wave/boundary layer interaction vortex develops downstream with curvature, while the converging main vortex develops downstream in a conical shape.

To visually demonstrate the fluid motion following vortices within the interaction regions, streamlines were traced downstream at different height layers in the inlet plane of the flow field. This yielded the spatial streamline distributions (Figure 17, right panel). The blue and red streamlines represent the results of tracing streamlines downstream from the z = 1 mm and z = 10 mm height layers, respectively. It can be observed that the streamlines originating from the bottom layer (z = 1 mm) are lifted upward after being disturbed and develop downstream in a spiral-shaped structure, indicating separation of the bottom-layer flow. In contrast, streamlines originating from the upper layer (z = 10 mm) are first lifted upward and then reattach downward near the corner region, demonstrating reattachment of the upper-layer fluid.

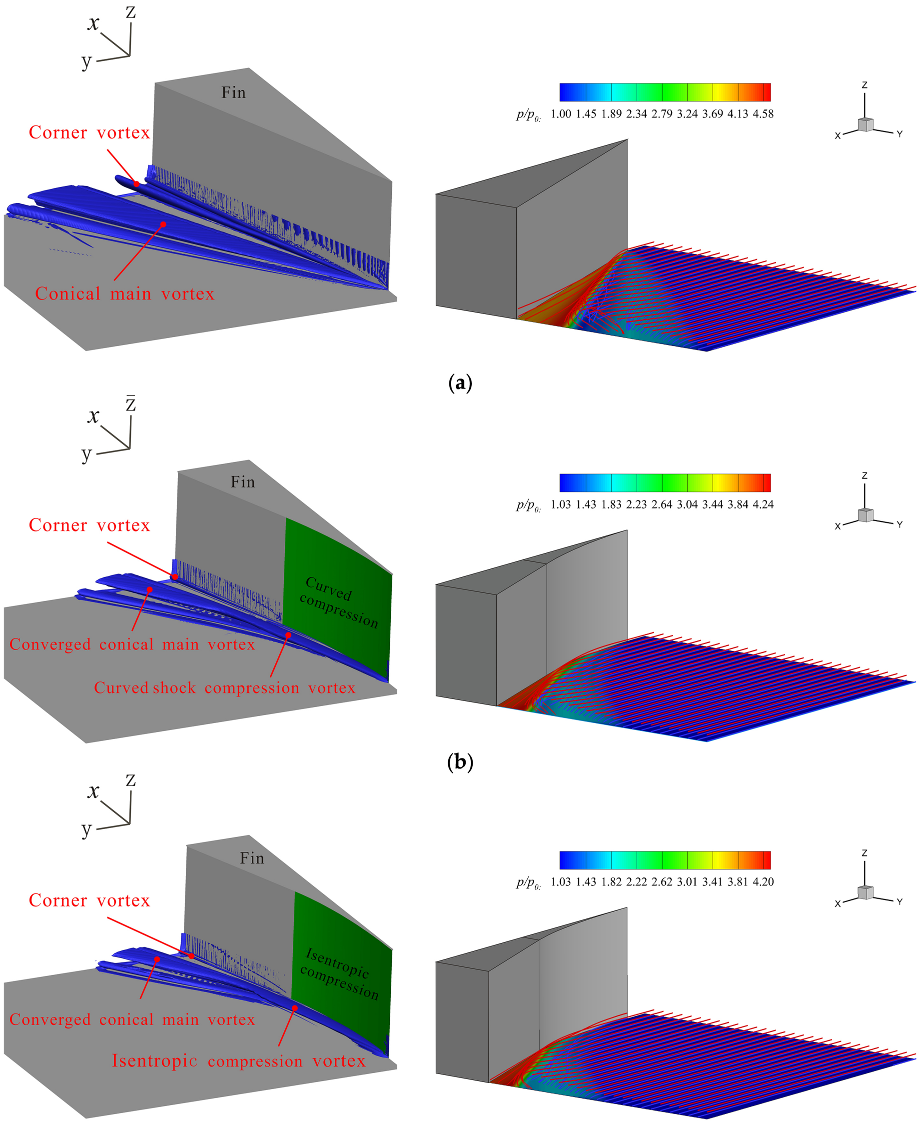

(**a**)

(**b**)

(**c**)

**Figure 17.** Comparisons of 3D vortex structures and streamline distributions ($Q^* = 6.08 \times 10^{-5}$). (**a**) Planar swept shock/turbulent boundary layer interaction. (**b**) Curved swept shock/turbulent boundary layer interaction. (**c**) Isentropic swept compression wave/turbulent boundary layer interaction.

Figure 18 presents the *Q*-criterion contours on the downstream cross-section near the outlet of the computational domain ($x$ = 500 mm) for different interaction regions. The cross-sectional envelopes of the main vortex and corner vortex can be identified from the contours. The normal scale of a vortex is defined as the distance from the plate surface to the highest point of the vortex envelope in the z-direction. As shown in Figure 13, the vortex envelopes remain nearly unchanged when $Q^* \leq 6.08 \times 10^{-5}$, indicating that $Q^* = 6.08 \times 10^{-5}$ is an appropriate threshold for vortex visualization. Comparison reveals that the planar SSWTBLI generates the largest main vortex and corner vortex scales, with their normal scales at the computational domain exit reaching $6.7\delta_0$ and $7.5\delta_0$, respectively. Curved compression yields the next largest scales, with normal scales of $5.4\delta_0$ for the main vortex and $1.8\delta_0$ for the corner vortex; Isentropic compression produces the smallest scales, with normal scales of $4.9\delta_0$ for the main vortex and $1.2\delta_0$ for the corner vortex.

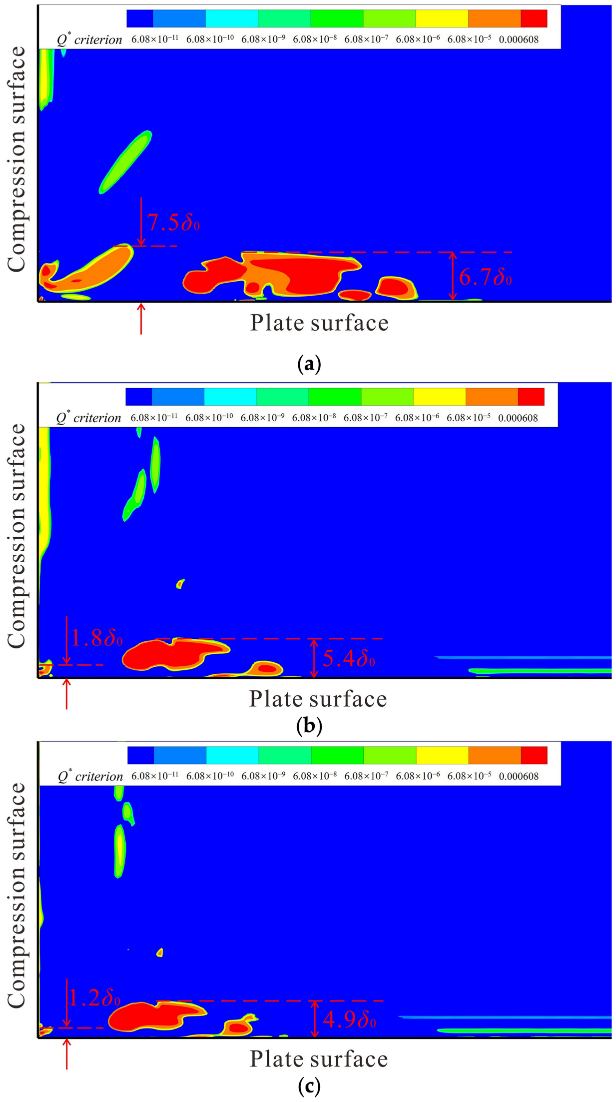

**Figure 18.** Q-criterion contours for different interaction regions (cross-section at $x$ = 500 mm). (**a**) Planar swept shock/turbulent boundary layer interaction. (**b**) Curved swept shock/turbulent boundary layer interaction. (**c**) Isentropic swept compression wave/turbulent boundary layer interaction.

The influence of the measurement-section location on the vortex-scale ranking was further examined. As shown in Figure 19, the horizontal axis denotes the measurement section location, and the vertical axis represents the vortex normal scale. The normal scales of both the primary vortex and the corner vortex increase gradually as the measurement section moves downstream. At each measurement section, the ranking of the vortex wall-normal scales remains unchanged among the different configurations, demonstrating the robustness of the vortex-scale ranking reported in this study.

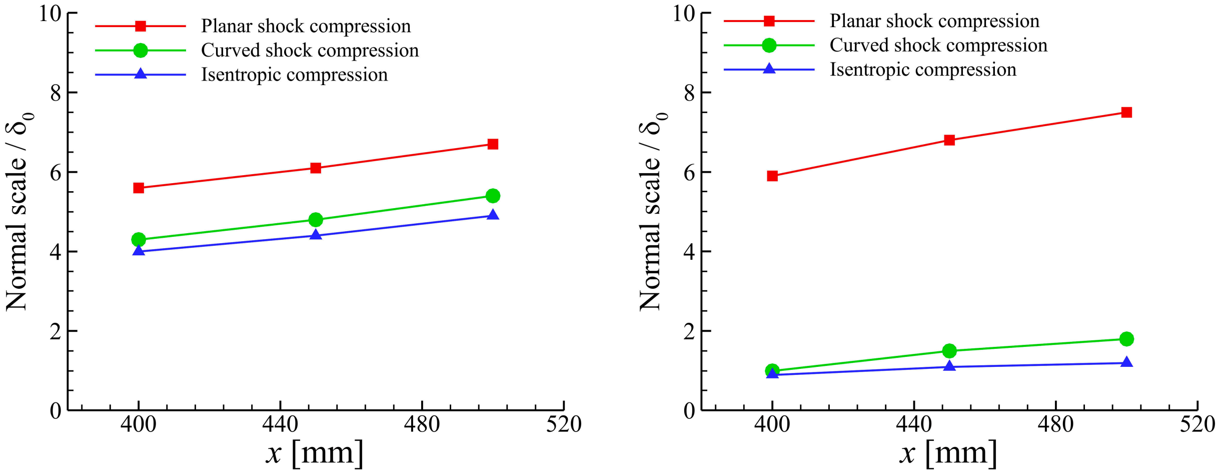

(**a**) (**b**)

**Figure 19.** Variation in vortex normal scale with the measurement section. (**a**) Primary vortex. (**b**) Corner vortex.

In addition, the influence of mesh sensitivity on the vortex normal scale has been further evaluated. Based on the results obtained using the fine and dense meshes, the normal scales of the primary vortex and corner vortex were compared. The results show that the relative error of the primary vortex normal scale between the fine and dense meshes is 0, while that of the corner-vortex normal scale is 2.9%, as shown in Table 4. These results indicate that the predicted vortex normal scales are stable and reliable under the present grid resolution.

**Table 4.** Comparison of vortex normal scales for different grids.

| | **Fine Grid** | **Dense Grid** | **Relative Error** |
|---|---|---|---|
| Primary vortex | $5.38\delta_0$ | $5.38\delta_0$ | 0.0% |
| Corner vortex | $1.77\delta_0$ | $1.72\delta_0$ | 2.9% |

To further investigate the effects of different compression configurations on the wave structure and aerodynamic parameters within the interaction region, two cross-sections perpendicular to the compression surface of the fin were extracted. These cross-sections align with Line 1 and Line 2 in Figure 12, and Mach number contour plots for both sections are presented in Figure 20. Figure 20 numerically labels typical flow structures within the interaction region. For the planar swept shock compression, the interaction region exhibits a typical λ-wave structure and a primary vortex beneath the λ-wave, with the primary vortex's scale significantly increasing downstream. For the curved swept shock compression, the entire interaction region comprises a swept curved shock, swept isentropic compression waves, separation compression waves, rear compression waves, and a main vortex. When the curved swept shock converges with the isentropic compression waves to form a converging planar shock, a slip line is generated within the interaction region. The other flow structures within this region are identical to those in planar swept shock compression. For the isentropic swept compression, only isentropic compression waves exist above the interaction region, including swept isentropic compression waves, separation compression waves, and rear compression waves, while a small-scale main vortex exists below the interaction region. When isentropic compression waves converge to form a converging planar shock, a slip line, λ waves, and a main vortex structure also form in the interaction region. Comparing the lateral flow structures reveals that at the same flow direction position, the main vortex and wave system structures formed by the planar swept shock/boundary layer interaction have the largest scale, followed by the curved swept shock, with the isentropic swept compression wave having the smallest scale.

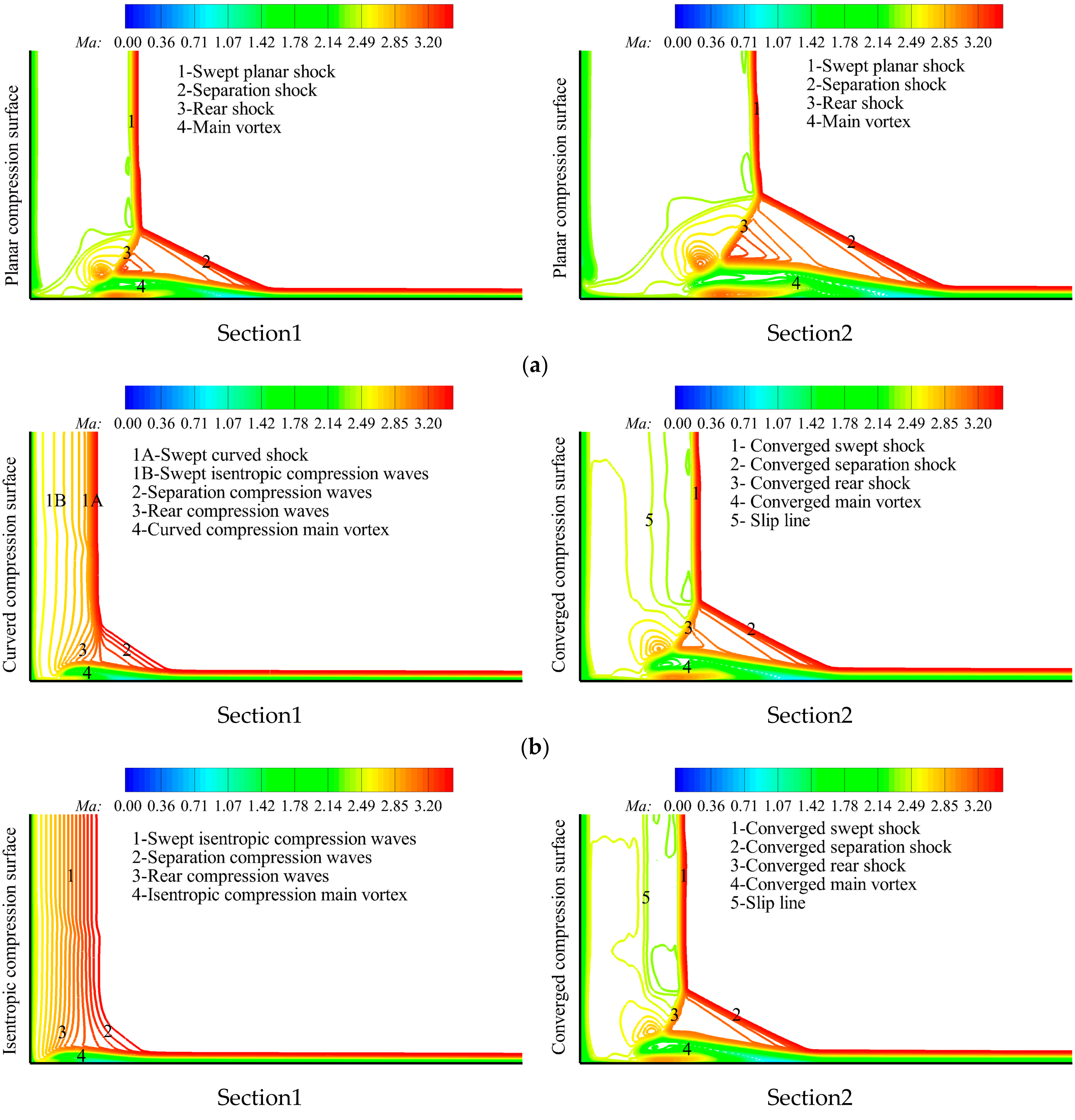

(a)

(b)

(c)

**Figure 20.** Comparison of Lateral Flow Structures. (**a**) Planar swept shock/turbulent boundary layer interaction. (**b**) Curved swept shock/turbulent boundary layer interaction. (**c**) Isentropic swept compression wave/turbulent boundary layer interaction.

### *3.3. Guidance for Inlet Design*

To investigate the effects of different compression configurations on macroscopic aerodynamic parameters within the interaction region, thereby providing guidance for the design of the external compression section of a supersonic inlet, a section perpendicular to

https://doi.org/10.3390/aerospace13060539

the compression surface was extracted at the convergence point of the shock/compression waves. Aerodynamic parameters within this section were extracted, with their specific location indicated as "Section_in" in Figure 21. In practical inlet design, the shock-convergence point generally coincides with the inlet lip location, namely the inlet entrance plane. Moreover, the convergence points of the three configurations in Figure 21 are located at the same streamwise distance of 400 mm from the computational domain inlet. Therefore, the shock-convergence section was selected as the common reference plane for comparing the three configurations. In practice, "Section_in" can be regarded as the entrance of the inlet, and the area "Ac" corresponding to "Section_in" represents the inlet capture area.

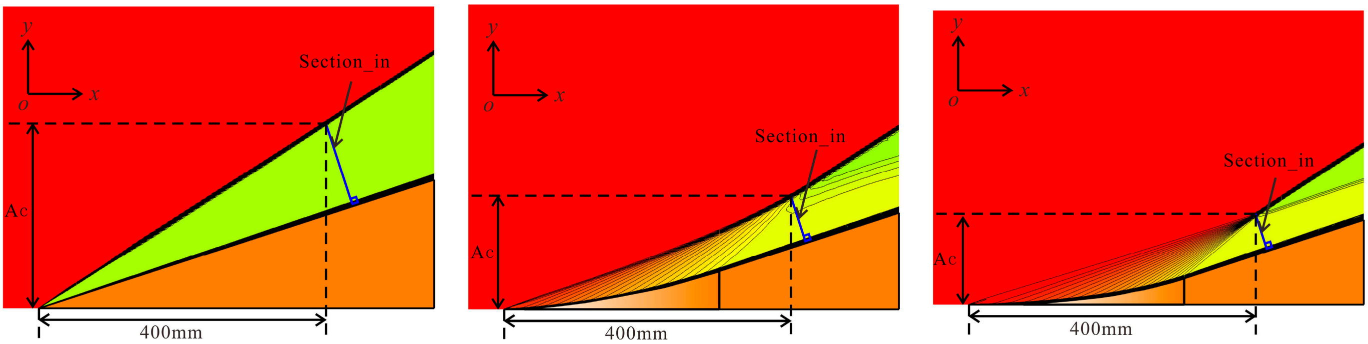

(**a**) (**b**) (**c**)

**Figure 21.** Sketch of Section Positions. (**a**) Planar shock compression. (**b**) Curved shock compression. (**c**) Isentropic compression.

In this paper, two dimensionless parameters, compression surface compression efficiency $\eta_\mathrm{p}$ and compression surface flow capture efficiency $\eta_\varphi$, are defined to compare the comprehensive efficiency of the three compression configurations, and their calculation expressions are given as follows.

$$\eta_\mathrm{p} = \pi\sigma \tag{6}$$

$$\eta_\varphi = \frac{\varphi A_\mathrm{c}}{S} \tag{7}$$

where $\pi$ is the pressure ratio, $\sigma$ is the total pressure recovery coefficient, and $\eta_\mathrm{p}$ is the compression surface compression efficiency, whose physical meaning is the product of the pressure ratio and the total pressure recovery coefficient of the compression surface. $\varphi$ represents the flow coefficient, $A_\mathrm{c}$ denotes the capture area, $S$ is the total surface area of the compression surface involved in airflow compression and flow capture, and $\eta_\varphi$ signifies the compression surface flow capture efficiency, whose physical meaning is the flow capture efficiency per unit area of the compression surface along the flow direction. Achieving efficient compression of maximum flow with minimal surface area benefits thermal protection, drag reduction, and structural weight reduction in aircraft. Therefore, $\eta_\mathrm{p}$ and $\eta_\varphi$ serve as crucial metrics for evaluating the design quality of the inlet within both the powerplant and aircraft systems.

Table 5 presents the aerodynamic performance metrics of the three compression configurations, with all parameters obtained using mass-flow-weighted averaging. The comparison shows that the pressure ratio and flow coefficient differ only slightly among the three compression configurations, whereas the total pressure recovery exhibits more pronounced differences. The isentropic compression configuration achieves the highest total pressure recovery, followed by the curved shock compression configuration, while the planar-shock compression configuration shows the lowest value. Based solely on the conventional metrics ($\pi$, $\sigma$, $\varphi$), the isentropic compression configuration demonstrates the best overall aerodynamic performance.

**Table 5.** Comparison of aerodynamic performance metrics for Three Swept Compression Configurations.

| Compression Types | Planar Shock Compression | Curved Shock Compression | Isentropic Compression |
|---|---|---|---|
| $\pi$ | 3.90 | 3.96 | 4.06 |
| $\sigma$ | 0.775 | 0.937 | 0.954 |
| $\varphi$ | 0.964 | 0.973 | 0.972 |
| $A_c/S$ | 0.560 | 0.365 | 0.293 |
| $\eta_p$ | 3.023 | 3.709 | 3.868 |
| $\eta_\varphi$ | 0.540 | 0.356 | 0.285 |

When the compression efficiency and flow capture efficiency are further considered, the isentropic compression configuration still exhibits the highest compression efficiency, followed by the curved shock compression configuration and then the planar shock compression configuration. However, the isentropic compression configuration has the lowest flow capture efficiency, whereas the planar shock compression configuration achieves the highest. A higher compression efficiency can increase the inlet exit total pressure recovery and pressure ratio, thereby improving the installed thrust of the engine. However, a lower flow capture efficiency may increase the structural weight and drag of the aircraft platform. Therefore, in practical inlet design, both the compression efficiency and the flow-capture efficiency of the compression surface should be considered when selecting an appropriate compression configuration.

It should be noted that $\eta_\varphi$ is not intended to negate the aerodynamic advantages of the isentropic compression configuration. In fact, the isentropic compression configuration achieves the highest total pressure recovery, indicating its clear advantage in reducing total pressure losses. However, because it has the largest compression surface area $S$ involved in flow compression and capture, its $\eta_\varphi$ value is relatively low. This indicates that the higher total pressure recovery and compression efficiency of the isentropic compression configuration are achieved at the cost of a larger compression surface. Therefore, $\eta_\varphi$ is more appropriately regarded as a supplementary engineering metric that reflects the trade-off between aerodynamic performance and geometric/structural cost. As shown in Table 5, the curved shock compression provides a balanced compromise between compression efficiency and flow capture efficiency under the present conditions, suggesting its potential as a candidate for further inlet design optimization.

## 4. Conclusions

The interaction between swept compression waves and sidewall boundary layers, a phenomenon critical to the forebody and cowl flows of hypersonic inlets, is simplified through a canonical fin-plate configuration. Numerical simulations are conducted to elucidate the flow physics of interactions induced by three distinct compression mechanisms: planar swept shocks, curved swept shocks, and continuous isentropic compression waves. The principal conclusions derived from this study are summarized as follows:

(1) The interactions induced by both curved swept shocks and isentropic swept compression depart from the classical conical similarity typically associated with planar configurations. However, downstream of the shock wave coalescence, the flow recovers its conical similarity within the resultant interaction region. Furthermore, the topological characteristics of separation in curved-compression interactions deviate from the classification framework established by Alvi and Settles [10,11], challenging the applicability of this conventional theory to non-planar swept compression systems.

(2) Both curved shock and isentropic compression interactions induce large-scale primary vortices that evolve along curved trajectories downstream, accompanied by small-scale corner vortex structures. At a consistent total deflection angle, the baseline planar SSWTBLI exhibits the largest spatial extent for both vortex structures, with normal scales reaching $6.7\delta_0$ and $7.5\delta_0$, respectively. In comparison, curved shock compression results in reduced normal scales of $5.4\delta_0$ and $1.8\delta_0$. Isentropic compression manifests the most compact separation, with the minimum normal scales measured at $4.9\delta_0$ for the primary vortex and $1.2\delta_0$ for the corner vortex.

(3) Comparative analysis of compression efficiency and flow capture efficiency across the three swept compression configurations reveals a significant performance trade-off. While isentropic compression yields the maximum compression efficiency, it simultaneously results in the minimum flow capture efficiency. Conversely, planar shock compression provides superior flow capture at the expense of compression efficiency. In the aerodynamic design of high-speed inlets, a comprehensive evaluation of these competing metrics is required for selecting the optimal compression topology. Curved shock compression strikes a favorable balance between pressure gain and flow capture, emerging as a viable candidate for maximizing the integrated performance of the inlet system.

Comparative analysis of compression efficiency and flow capture efficiency across the three swept compression configurations reveals a significant performance trade-off. While isentropic compression yields the maximum compression efficiency, it simultaneously results in the minimum flow capture efficiency. Conversely, planar shock compression provides superior flow capture at the expense of compression efficiency. In the aerodynamic design of high-speed inlets, a comprehensive evaluation of these competing metrics is required for selecting the optimal compression topology. Within the present parametric space, curved shock compression strikes a favorable balance between pressure gain and flow capture, suggesting its potential as a candidate for further inlet design optimization rather than a universally optimal configuration. Further investigations over broader operating conditions, wall thermal boundary conditions, and practical inlet geometries are required before making more general design recommendations.

**Author Contributions:** Conceptualization, F.S. and H.T.; Methodology, F.S. and D.S.; Software, D.S.; Validation, D.S.; Formal analysis, X.L.; Investigation, X.L.; Resources, H.H.; Writing—original draft, F.S. and X.L.; Writing—review & editing, H.T.; Supervision, H.H., H.T. and Z.Z.; Project administration, H.H. and Z.Z.; Funding acquisition, Z.Z. All authors have read and agreed to the published version of the manuscript.

**Funding:** This work was funded by the National Natural Science Foundation of China (Grant No. U25B2085 and 12532017).

**Data Availability Statement:** The raw data supporting the conclusions of this article will be made available by the authors on request.

**Acknowledgments:** The authors would like to acknowledge the High-Performance Computing Platform of Nanjing University of Aeronautics and Astronautics for providing high-performance computing (HPC) resources that have contributed to the research results in this paper.

**Conflicts of Interest:** Authors Fajia Sheng, Xiankai Li and Zhiyu Zhang were employed by the company Yangzhou Collaborative Innovation Research Institute Co., Ltd. The remaining authors declare that the research was conducted in the absence of any commercial or financial relationships that could be construed as a potential conflict of interest.

## References

1. Panaras, A.G. Review of the physics of swept-shock/boundary layer interactions. *Prog. Aerosp. Sci.* **1996**, *32*, 173–244. [CrossRef]
2. Huang, H.; Tan, H.; Li, F.; Tang, X.; Qin, Y.; Xie, L.B.; Xu, Y.Y.; Li, C.; Gao, S.; Zhang, Y.; et al. A review of the shock-dominated flow in a hypersonic inlet/isolator. *Prog. Aerosp. Sci.* **2023**, *143*, 100952. [CrossRef]
3. Huang, H.X.; Tan, H.J.; Sun, S.; Ling, Y. Evolution of supersonic corner vortex in a hypersonic inlet/isolator model. *Phys. Fluids* **2016**, *28*, 126101. [CrossRef]
4. McCabe, A. The three-dimensional interaction of a shock wave with a turbulent boundary layer. *Aeronaut. Q.* **1966**, *17*, 231–252. [CrossRef]
5. Korkegi, R.H. A simple correlation for incipient-turbulent boundary-layer separation due to a skewed shock wave. *AIAA J.* **1973**, *11*, 1578–1579. [CrossRef]
6. Korkegi, R.H. Comparison of shock-induced two-and three-dimensional incipient turbulent separation. *AIAA J.* **1975**, *13*, 534–535. [CrossRef]
7. Oskam, B.; Bogdonoff, S.M.; Vas, I.E. *Study of Three-Dimensional Flow Fields Generated by the Interaction of a Skewed Shock Wave with a Turbulent Boundary Layer*; Princeton University: Princeton, NJ, USA, 1975.
8. Zheltovodov, A.A.; Maksimov, A.I.; Schülein, E. Development of turbulent separated flows in the vicinity of swept shock waves. *Interact. Complex* **1987**, *3*, 67–91.
9. Deng, X.Y. Correlative behaviours of shock/boundary layer interaction induced by sharp fin and semicone. In Proceedings of the 22nd Fluid Dynamics, Plasma Dynamics and Lasers Conference, Honolulu, HI, USA, 24–26 June 1991. [CrossRef]
10. Alvi, F.S.; Settles, G. Structure of swept shock wave/boundary-layer interactions using conical shadowgraphy. In Proceedings of the 21st Fluid Dynamics, Plasma Dynamics and Lasers Conference, Seattle, WA, USA, 18–20 June 1990. [CrossRef]
11. Alvi, F.S.; Settles, G.S. Physical model of the swept shock wave/boundary-layer interaction flowfield. *AIAA J.* **1992**, *30*, 2252–2258. [CrossRef]
12. Knight, D.D.; Badekas, D.; Horstman, C.C.; Settles, G.S. Quasiconical flowfield structure of the three-dimensional single fin interaction. *AIAA J.* **1992**, *30*, 2809–2816. [CrossRef]
13. Rodi, P.E.; Dolling, D.S. Behavior of pressure and heat transfer in sharp fin-induced turbulent interactions. *AIAA J.* **1995**, *33*, 2013–2019. [CrossRef]
14. Fang, J.; Yao, Y.; Zheltovodov, A.A.; Lu, L. Investigation of three-dimensional shock wave/turbulent-boundary-layer interaction initiated by a single fin. *AIAA J.* **2017**, *55*, 509–523. [CrossRef]
15. Token, K.H. *Heat Transfer Due to Shock Wave Turbulent Boundary Layer Interactions on High Speed Weapon Systems*; Technical Report AFFDL-TR-74-77; Air Force Flight Dynamics Laboratory: Wright-Patterson AFB, OH, USA, 1974.
16. Kubota, H.; Stollery, J.L. An experimental study of the interaction between a glancing shock wave and a turbulent boundary layer. *J. Fluid Mech.* **1982**, *116*, 431–458. [CrossRef]
17. Bolton, J.T.; Thurow, B.S.; Alvi, F.S.; Arora, N. Single camera 3D measurement of a shock wave-turbulent boundary layer interaction. In Proceedings of the 55th AIAA Aerospace Sciences Meeting, Grapevine, TX, USA, 9–13 January 2017. [CrossRef]
18. Clifford, C.J.; Klemkowsky, J.N.; Thurow, B.S.; Arora, N.; Alvi, F.S. Visualization of an SBLI using Plenoptic BOS. In Proceedings of the 55th AIAA Aerospace Sciences Meeting, Grapevine, TX, USA, 9–13 January 2017. [CrossRef]
19. Jones, C.; Clifford, C.; Thurow, B.S.; Mears, L.; Arora, N.; Alvi, F.S. Two camera plenoptic PIV applied to shock wave-boundary layer interactions. In Proceedings of the 2018 Fluid Dynamics Conference, Atlanta, GA, USA, 25–29 June 2018. [CrossRef]
20. He, G.; Zhou, J.; Zhao, Y.X. Application of free interaction theory in swept shock wave/turbulent boundary layer interactions. *J. Vis.* **2018**, *21*, 203–214. [CrossRef]
21. Sheng, F.J.; Tan, H.J.; Zhuang, Y.; Huang, H.X.; Chen, H.; Wang, W.X. Visualization of conical vortex and shock in swept shock/turbulent boundary layer interaction flow. *J. Vis.* **2018**, *21*, 909–914. [CrossRef]
22. Dolling, D.S.; Bogdonoff, S.M. Upstream influence in sharp fin-induced shock wave turbulent boundary-layer interaction. *AIAA J.* **1983**, *21*, 143–145. [CrossRef]
23. Zheltovodov, A.A. Regimes and properties of three-dimensional separation flows initiated by skewed compression shocks. *J. Appl. Mech. Tech. Phys.* **1982**, *23*, 413–418. [CrossRef]
24. Degrez, G.; Ginoux, J.J. Surface phenomena in a three-dimensional skewed shock wave/laminar boundary-layer interaction. *AIAA J.* **1984**, *22*, 1764–1769. [CrossRef]
25. Dolling, D.S.; McClure, W.B. Flowfield scaling in sharp fin-induced shock wave/turbulent boundary-layer interaction. *AIAA J.* **1985**, *23*, 201–206. [CrossRef]
26. Dolling, D.S. Upstream influence in conically symmetric flow. *AIAA J.* **1985**, *23*, 967–969. [CrossRef]
27. Settles, G.S.; Lu, F.K. Conical similarity of shock/boundary-layer interactions generated by swept and unswept fins. *AIAA J.* **1985**, *23*, 1021–1027. [CrossRef]
28. Knight, D.D.; Horstman, C.C.; Shapey, B.; Bogdonoff, S. Structure of supersonic turbulent flow past a sharp fin. *AIAA J.* **1987**, *25*, 1331–1337. [CrossRef] [PubMed]

29. Kim, K.S.; Settles, G.S. Skin friction measurements by laser interferometry in swept shock/boundary-layer interactions. *AIAA J.* **1990**, *28*, 133–139. [CrossRef]
30. Hsu, J.; Settles, G. Holographic flowfield density measurements in swept shock wave/boundary-layer interactions. In Proceedings of the 30th Aerospace Sciences Meeting and Exhibit, Reno, NV, USA, 6–9 January 1992. [CrossRef]
31. Borovoy, V.; Egorov, I.; Mosharov, V.; Radchenko, V.; Skuratov, A.; Struminskaya, I. Entropy-layer influence on single-fin and double-fin/boundary-layer interactions. *AIAA J.* **2016**, *54*, 443–457. [CrossRef]
32. Li, X.K.; Sheng, F.J.; Li, J.W.; Yin, C.; He, M.F.; Zhou, H.; Liu, J. Investigation on Flow Characteristics of Swept Shock/Turbulent Boundary Layer Interaction Considering Entropy Layer Effect. *Phys. Gases.* **2023**, *8*, 1–14. [CrossRef]
33. Garrison, T.; Settles, G. Flowfield visualization of crossing shock-wave/boundary-layer interactions. In Proceedings of the 30th Aerospace Sciences Meeting and Exhibit, Reno, NV, USA, 6–9 January 1992. [CrossRef]
34. Garrison, T.J.; Settles, G.S.; Narayanswami, N.; Knight, D.D. Structure of crossing-shock-wave/turbulent-boundary-layer interactions. *AIAA J.* **1993**, *31*, 2204–2211. [CrossRef] [PubMed]
35. Thivet, F.; Knight, D.D.; Zheltovodov, A.A.; Maksimov, A.I. Insights in turbulence modeling for crossing-shock-wave/boundary-layer interactions. *AIAA J.* **2001**, *39*, 985–995. [CrossRef]
36. Thivet, F.; Knight, D.D.; Zheltovodov, A.A.; Maksimov, A.I. Analysis of observed and computed crossing-shock-wave/turbulent-boundary-layer interactions. *Aerosp. Sci. Technol.* **2002**, *6*, 3–17. [CrossRef]
37. Yao, Y.; Salin, A.; Lo, S. Numerical analysis of wall properties in crossing-shock-wave/turbulent-boundary-layer interactions. In Proceedings of the 49th AIAA Aerospace Sciences Meeting including the New Horizons Forum and Aerospace Exposition, Orlando, FL, USA, 4–7 January 2011. [CrossRef]
38. Salin, A.; Yao, Y.; Zheltovodov, A. Comparison and improvement of wall heat transfer prediction in crossing-shock-wave/turbulent-boundary-layer interaction conditions. In Proceedings of the 51st AIAA Aerospace Sciences Meeting including the New Horizons Forum and Aerospace Exposition, Grapevine, TX, USA, 7–10 January 2013. [CrossRef]
39. Jordan, C.; Edwards, J.R.; Stefanski, D.L. RANS closure model assessment using LES/RANS datasets for a hypersonic crossing-shock interaction. In Proceedings of the AIAA SCITECH 2022 Forum, San Diego, CA, USA, 3–7 January 2022. [CrossRef]
40. Sebastian, J.J.; Lu, F.K. Numerical investigation of separated flowfield in a crossing shockwave/laminar boundary-layer interaction. In Proceedings of the AIAA SCITECH 2022 Forum, San Diego, CA, USA, 3–7 January 2022. [CrossRef]
41. Seckin, S.; Mears, L.J.; Song, M.; Alvi, F.S.; Zigunov, F. Surface properties of double-fin generated shock-wave/boundary-layer interactions. *AIAA J.* **2023**, *61*, 5302–5319. [CrossRef]
42. Sheng, F.J.; Tan, H.J.; Huang, H.X.; Liu, Y.Z.; Gao, W.N.; Wang, W.X. Investigation on Flow Characteristics of Successive Bi-Swept Shock Waves/Turbulent Boundary Layer Interaction. *J. Propuls. Technol.* **2019**, *40*, 1023–1031. [CrossRef]
43. Sheng, F.J. Research on Characteristics of Ipsilateral Bi-Swept Shock Wave/Turbulent Boundary Layer Interactions. Master's Thesis, College of Energy and Power Engineering, Nanjing University of Aeronautics and Astronautics, Nanjing, China, 2019. [CrossRef]
44. He, G. Investigation on the Three-Dimensional Swept Impinging Oblique Shock/Turbulent Boundary Layer Interactions. Ph.D. Thesis, College of Aerospace Science and Engineering, National University of Defense Technology, Changsha, China, 2018. [CrossRef]
45. Panaras, A.G. The effect of the structure of swept-shock-wave/turbulent-boundary-layer interactions on turbulence modelling. *J. Fluid Mech.* **1997**, *338*, 203–230. [CrossRef]
46. Thivet, F.; Knight, D.D.; Zheltovodov, A.A.; Maksimov, A.I. Importance of limiting the turbulent stresses to predict 3D shock-wave/boundary-layer interactions. In Proceedings of the 23rd International Symposium on Shock Waves, Fort Worth, TX, USA, 22–27 July 2001.